ACS APPLIED MATERIALS & INTERFACES

www.acsami.org

Research Article

# Tuning the Microstructures of ZnO To Enhance Photocatalytic NO Removal Performances

Reshalaiti Hailili,* Xiaokaiti Reyimu, Zelong Li, Xu Lu, and Detlef W. Bahnemann*

Cite This: *ACS Appl. Mater. Interfaces* 2023, 15, 23185−23198

Read Online

ACCESS | Metrics & More | Article Recommendations | Supporting Information



**ABSTRACT:** Effective removal of kinetically inert dilute nitrogen oxide (NO, ppb) without $NO_2$ emission is still a challenging topic in environmental pollution control. One effective approach to reducing the harm of NO is the construction of photocatalysts with diversified microstructures and atomic arrangements that could promote adsorption, activation, and complete removal of NO without yielding secondary pollution. Herein, microstructure regulations of ZnO photocatalysts were attempted by altering the reaction temperature and alkalinity in a unique ionic liquid-based solid-state synthesis and further investigated for the removal of dilute NO upon light irradiation. Microstructure observations indicated that as-tuned photocatalysts displayed unique nucleation, diverse morphologies (spherical nanoparticles, short and long nanorods), defect-related optical characteristics, and enhanced carrier separations. Such defect-related surface−interface aspects, especially $V_o''$-related defects of ZnO devoted them to the 4.16-fold enhanced NO removal and 2.76 magnitude order decreased $NO_2$ yields, respectively. Improved NO removal and toxic product inhabitation in as-tuned ZnO was disclosed by mechanistic exploitations. It was revealed that regulated microstructures, defect-related charge carrier separation, and strengthened surface interactions were beneficial to active species production and molecular oxygen activation in ZnO, subsequently contributing to the improved NO removal and simultaneous avoidance of $NO_2$ formation. This investigation shed light on the facile regulation of microstructures and the roles of surface chemistry in the oxidation of low concentration NO in the ppb level upon light illumination.

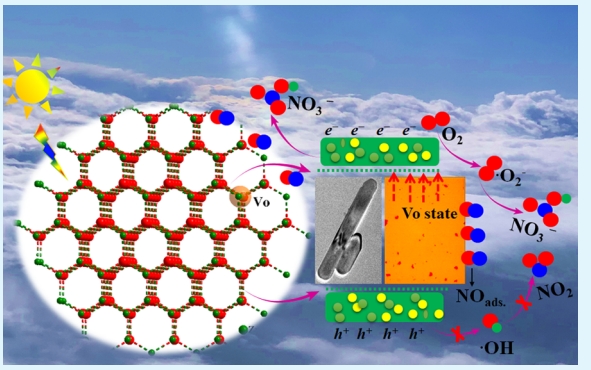


**KEYWORDS:** *photocatalysis, microstructure, surface interface, carrier separation, NO removal*

## 1. INTRODUCTION

Nowadays, air pollution has become a globally prominent environmental problem, in which nitrogen oxide ($NO_x$, 95% NO, and $NO_2$) has been considered one of the most serious harmful gaseous pollutants that can cause haze, photochemical smog, and acid rain.[1] Exposure to NO (~ppb) harms human health with a risk for respiratory and cardiopulmonary diseases.[2] According to the WHO (World Health Organization) guideline, the lowest $NO_x$ concentration emission threshold under the current was set at 40 $\mu g \cdot m^{-3}$.[3] Conventionally, methods, e.g., physical/chemical adsorption, advanced wet oxidation, and postcombustion reduction technologies such as selective catalytic reduction with $NH_3$ (SCR-$NH_3$) and hydrocarbons (SCR-HC), are used for minimizing the NO emission.[4−6] However, these approaches require high temperatures, special handling systems, and sophisticated equipment to avoid $NH_3$ slip, reducing agents, or cocatalysts, meanwhile suffering from high costs and yields of more toxic byproducts, no longer applicable for the removal of dilute NO. Semiconductor-based photocatalysis has received considerable attention to treat atmospheric gaseous hazards in low concentration though with higher toxicity, e.g., NO (ppb level), in an economically attractive and environmentally friendly manner.[7−10] Although huge efforts are devoted to rescuing photocatalytic NO removal, the reaction efficiency still remains low, as the generation of more toxic intermediates (e.g., $NO_2$ and $N_2O$), and cannot meet the requirements of complete NO removal. Thus, it is highly desirable to design and explore photocatalysts exhibiting high efficiency for NO conversion and inhibiting toxic byproduct yields to avoid secondary pollution. Witnessed efforts demonstrate that microstructure controlling, e.g., strengthening surface−interface interaction and promoting carrier separations on pure photocatalyst, is the most ideal and useful method to enhance reaction efficiency, which is still mostly desired and challenging.[11−14]

**Received:** February 16, 2023
**Accepted:** April 12, 2023
**Published:** May 2, 2023

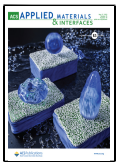




https://doi.org/10.1021/acsami.3c02286
*ACS Appl. Mater. Interfaces* 2023, 15, 23185−23198

With higher carrier mobility and optical excitations than the famous star catalyst $TiO_2$, zinc oxide (ZnO) is proven to be superior for environmental pollution control, e.g., pollutant degradation, water splitting, and so on.[15−17] Even though ZnO is widely investigated for pollutant degradations, the reaction efficiency in such wet reactions appears far from satisfactory due to the concerns on catalyst stability and charge carrier separation, which need to be explored thoroughly. Doping with transition metals or morphological evolution appears to tackle such limitations, though also leads to undesirable instability and low reaction yields.[18−20] Recent knowledge about the photocatalytic utility of ZnO indicated that its reaction efficiency could be improved in the gas−solid system such as photocatalytic $CO_2$ reduction, NO removal, and no longer suffers from undesirable photocorruption, catalysts deactivation, and sluggish charge carrier recombination.[21−25] Theoretically, the key strategy for improving the NO removal over ZnO photocatalysts is to vary the surface interactions by strong electrostatic interactions between the catalyst's surfaces and NO molecules. Our recent investigation clarified that precise tuning of the surface defects on the surfaces of ZnO could promote complete NO (∼ppb) oxidations, providing the hard evidence to disclose significant roles of defect-induced surface interface controlling for the probe molecule adsorption, dissociation of reactants, electron transfer behaviors, and surface reactivity.[24] Hence, changing the surface interaction of ZnO is an effective way to improve the photocatalytic NO conversion due to its unique crystal structure and distinct surface aspects, which deserve to receive more attention. Structurally, ZnO is composed of fourfold tetrahedrally coordinated $O_2^-$ and $Zn^{2+}$ ions stacked alternatively along the *c*-axis. The positively charged Zn-terminated and negatively charged O-terminated polar surfaces in ZnO resulted in spontaneous polarization and variations of the surface structure. Evidently, surface structures of ZnO can be tuned in unique fabrications by using organic templates or solvents, which could compensate for surface charges, promote effective adsorptions of probe molecules, and subsequently enhance photocatalytic performances.[26,27] Comprised of both a hydrophilic ionic head group and a hydrophobic organic chain and acquired superior physical properties of negligible vapor pressures, wide liquidus ranges, tunable solubility, and flexibility, ionic liquids are known as effective solvents for microstructure controlling of materials.[28] Our recent study indicates that the photocatalytic reactivity of perovskites is improved through microstructure regulations in ionic liquid-assisted preparations.[29] It is, however, desirable to bear how different microstructures of ZnO are being controlled and govern further applications. Hence, systematic investigations on microstructure controlling of ZnO and their implementations for air purification still require a great deal of effort.

Taking advantage of unique crystal structures and potential applications in environmental pollution control, microstructure regulations of ZnO were attempted using an ionic liquid-based solid-state method to investigate the roles of surface interfaces for photocatalytic NO removal. By varying temperature and alkalinity in the ionic liquid atmosphere, the microstructure regulations of ZnO were achieved, and the growth mechanisms of such diverse structures were further explored. As-regulated ZnO photocatalysts were further utilized for the photocatalytic NO removal to disclose the roles of tuned microstructure. Results showed that microstructure manipulations in ZnO could exert enhanced efficiency with 55.45% NO removal and suppressed $NO_2$ yield with 33% reaction selectivity. Finally, the true mechanism for microstructures-mediated enhanced NO removal with suppressed $NO_2$ yields over as-tuned ZnO was inspected by a series of mechanistic investigations.

## 2. EXPERIMENTAL SECTION

**2.1. Preparations.** *2.1.1. Synthesis of Ionic Liquid.* 1-Ethyl-3-methylimidazolium iodide ([Bmin]I, Scheme 1) was prepared according to our recent work.[29] In a typical synthesis, a mixture of Iodobutane (0.80 mol) and 1-methylimidazole (0.80 mol) was stirred at 70 °C for 56 h until two phases formed. The top phases, containing unreacted starting material, were decanted and ethyl acetate was added with thorough mixing. The ethyl acetate was decanted followed by the addition of fresh ethyl acetate, and this step was repeated twice. Washing with ethyl acetate should suffice to remove any unreacted material from the bottom phase. After the third decanting of ethyl acetate, any remaining ethyl acetate was removed and stirred while on a vacuum line. All other steps remain the same.

**Scheme 1. Crystal Structure and Images of As-Synthesized Ionic Liquid 1-Ethyl-3-methylimidazolium Iodide ([Bmim]I)**

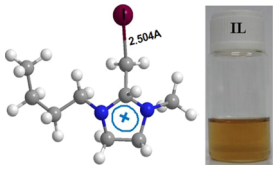


*2.1.2. Preparation of Photocatalysts.* ZnO photocatalysts were synthesized by a one-step low-temperature solid-state route. In a typical synthesis of sample 1, precisely measured zinc acetate ($Zn(CH_3COO)_2{\cdot}2H_2O$, 4.0 mmol) was ground for about 45 min in an agate mortar, followed by the addition of 2.0 g as-synthesized ionic liquid [Bmin]I and sodium hydroxide (NaOH, 24.0 mmol, undergo 30.0 min ground) powder, respectively. In the final step, the mixture was ground for 40 min and heated at 60 °C for 48 h to complete the crystallization process. Then, it was washed with the mixture of alcohol/water and dried in a heating oven at 60 °C. The detailed preparations of other samples were the same with sample 1 except that the different reaction temperatures (60, 80, and 100 °C) and alkalinity ($[Zn^{2+}]/[OH^-]$ = 1:2, 1:4, and 1:6) were varied.

**2.2. Characterization.** Microstructures of the as-tuned photocatalysts were observed by scanning electron microscopy (SEM, Hitachi S-3500 N), transmission electron microscopy (TEM, JEOL JEM 2010), and high-resolution transmission electron microscopy (HRTEM), respectively. The atomic structures of as-regulated ZnO were characterized by double-aberration corrected high-angle annular dark-field scanning TEM (HAADF-STEM; JEOL JEM-2200FS). Specific surface areas of as-regulated photocatalysts (45.0 mg/per) were determined by the Brunauer−Emmett−Teller (BET) method and calculated from the linear part of the multipoint BET plot. Before the measurements, as-obtained powder samples were pretreated at 120 °C for 180 min, and $N_2$ adsorption−desorption isotherms were recorded with a QUADRASORB IQ (Quantachrome Instrument Corp). Crystal structures and phase confirmations were analyzed by X-ray diffraction (XRD) using a Bruker AXS D8 Advance diffractometer operating with a graphite monochromator set for Cu K$\alpha$ radiation ($\lambda$ = 1.5418 Å, 40.0 kV, and 30.0 mA) with the angular $2\theta$ range of 3°−80°. Surface chemical compositions, electronic states, and valence band (VB) positions were conducted using an X-ray photoelectron spectroscopy (XPS, Thermo Scientific ESCALab250-Xi) using 200 W monochromatic Al K$\alpha$ radiation. The 500 $\mu$m X-ray spot was used for SAXPS analysis, and the hydrocarbon C 1s line at 284.8 eV from adventitious carbon was used for energy referencing.

**2.3. Photocatalytic Activity Investigations.** To evaluate and further explore how the regulated microstructures influence the


https://doi.org/10.1021/acsami.3c02286
ACS Appl. Mater. Interfaces 2023, 15, 23185−23198

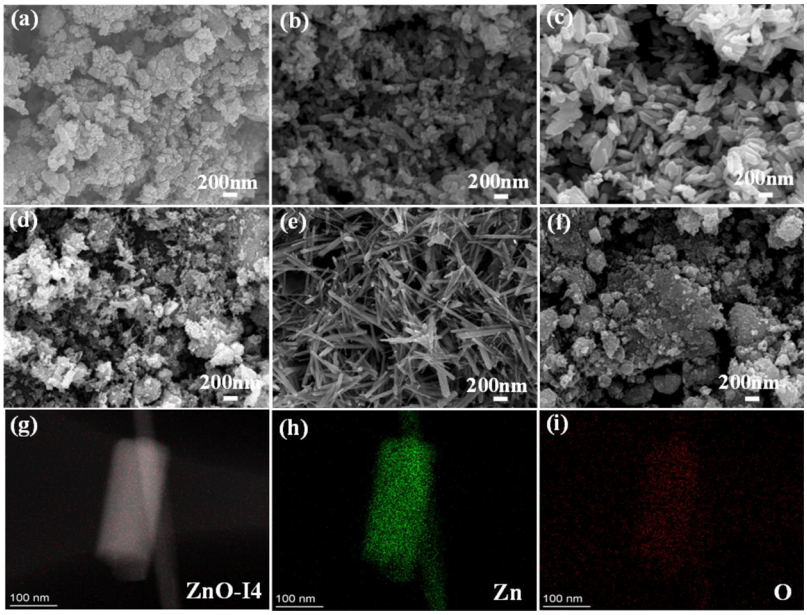


**Figure 1.** SEM images of (a) sample 1 (60 °C, 1:4); (b) sample 2 (80 °C, 1:4); (c) sample 3 (100 °C, 1:4); (d) sample 4 (100 °C, 1:2); (e) sample 5 (100 °C, 1:6); and (f) reference ZnO obtained in an ionic liquid free system (100 °C, 1:6), respectively; and (g–i) elemental mapping exhibiting uniform element distribution on the surfaces of sample 3.

photocatalytic activity of ZnO, the potential gaseous pollutant NO (in ppb level) was selected as a typical probe model for oxidation reactions. A continuous-flow setup equipped with an online chemiluminescence-based $NO_x$ analyzer (Thermo Scientific, $NO_x$ analyzer, model 42i-DNMSDAA), with a measurement range of 0.0–2.0 ppm, was used according to our previous work.[24] The specially designed quartz glass was used as the main reactor, above which a 300 W Xe lamp (PLS-SXE300, Perfect Light, Beijing, China) was arranged as a main light source. The details of the photocatalytic NO conversion experiments are given in the Supporting Information, SI. The concentration variations of $NO_2$ were simultaneously calculated from concentration gaps between NO and $NO_x$ during the tests. The corresponding NO removal efficiency, $NO_x$ conversions (%), and $NO_2$ selectivity were obtained by the following equation:[26]

$$\text{NO conversion } (\varphi_{NO}, \%) = (1 - \{[NO]_{in}/[NO]_{out}\}) \times 100\%$$

$$NO_x \text{ conversion } (\eta_{NOx}, \%) = ([NO_x]_{in} - [NO_x]_{out})/[NO_x]_{in} \times 100\%$$

$$NO_2 \text{ selectivity } (S_{NO2}, \%) = [NO_2]_{out}/([NO]_{in} - [NO]_{out}) \times 100\%$$

where $[NO]_{in}$, $[NO]_{out}$ are the initial and final concentrations of NO, while $[NO_x]_{in}$, $[NO]_{out}$, and $[NO_2]_{out}$ represent the initial and final concentrations of $NO_x$ and $NO_2$ in the ppb level, respectively.

**2.4. Structure–Property Correlations Investigations.** *2.4.1. Electrooptical Properties.* Optical responses of as-tuned ZnO photocatalysts were investigated by UV–vis diffuse reflection spectra (DRS) analyses. In typical tests, the dry-pressed disk samples with identical amounts (30.0 mg) were diluted with a standard reference $BaSO_4$, and optical responses were collected from 200 to 800 nm using a scan UV–vis spectrophotometer (UV–vis DRS UV-2450, Shimadzu, Japan) equipped with an integrating sphere assembly. The photoluminescence (PL) spectra were recorded on an FLS1000 Photoluminescence Spectrometer, Edinburgh Instruments Ltd. with a 300 W Xe lamp.

*2.4.2. Photo-Electrochemical Tests.* The photocurrent and electrochemical impedance spectroscopy (EIS) investigations were performed on an electrochemical workstation (CHI 600E) with a standard three-electrode system, in which Pt was used as a counter electrode. Ag/AgCl electrodes in KCl saturated solution were employed as reference electrodes, and the catalyst-deposed indium-tin-oxide (ITO) glass substrates with an area of 1.0 × 1.0 $cm^2$ were used as working electrodes, respectively. A 0.20 M $Na_2SO_4$ solution was used as the electrolyte, and 300 W Xenon lamp was used as a light source in the activity assessment test.

*2.4.3. Active Species Confirmation and Radical Trapping Tests.* To confirm qualitative productions of photocatalytically active species and their roles in photocatalytic NO removal, ESR spin trapping tests, and radical hunting investigations were operated on the ZnO photocatalyst. The details of the photocatalytic NO conversion experiments are given in the SI.

## 3. RESULTS AND DISCUSSION

**3.1. Microstructure Observation of ZnO Photocatalysts Prepared in Ionic Liquid [Bmim]I.** Microstructure regulations of ZnO were attempted by an environmentally friendly, cost-effective ionic liquid-assisted low-temperature solid-state synthesis. Figure 1 shows specific microstructures of ZnO obtained with the addition of ionic liquid [Bmim]I by varying reaction temperatures (60–100 °C) and alkalinity ($[Zn^{2+}]/[OH^-]$ = 1:2–1:6), respectively. The influences of temperature on the catalyst's structure were investigated first with relatively moderate alkalinity ($[Zn^{2+}]/[OH^-]$ was fixed as 1:4). Interestingly, as-studied ZnO exhibit diversified microstructures with clear/rough surfaces. Uniformly dispersed spherical nanoparticles (20–40 nm) were captured under relatively lower conditions (60 °C, sample 1, Figure 1a). When the reaction temperature was increased to 80 °C and other changes kept the same, the samples exhibited very short nanorods with an average length of 200–400 nm and diameters of 20–40 nm, respectively (sample 2, Figure 1b). Furthermore, when the reaction temperature further increased to 100 °C, individual short nanorods with average lengths and diameters of 300–500 and 50–100 nm are observed in sample 3, respectively (Figure 1c). As observed, the microstructures of ZnO varied based on the reaction temperature even with identical $[Zn^{2+}]/[OH^-]$ and ionic liquid addition. Based on these microstructure changes, we


https://doi.org/10.1021/acsami.3c02286
ACS Appl. Mater. Interfaces 2023, 15, 23185–23198

Table 1. Synthesis and Microstructure Characters of ZnO Photocatalysts Regulated in [Bmim]I

| sample | $[OH^-]/[Zn^{2+}]$ (molar ratio) | reaction temperature (°C) | microstructure | average diameter (nm) | length (nm) | aspect ratio ($L/D$) |
|---|---|---|---|---|---|---|
| 1 | 4 | 60 | nanoparticles | 20−40 | 30−50 | 1.5 |
| 2 | 4 | 80 | short nanorods | 20−40 | 200−400 | 10 |
| 3 | 4 | 100 | short nanorods | 30−50 | 300−500 | 10 |
| 4 | 2 | 100 | nanoparticles | 20−40 | 40−60 | 2 |
| 5 | 6 | 100 | long nanorods | 300−500 | 3000−5000 | 10 |

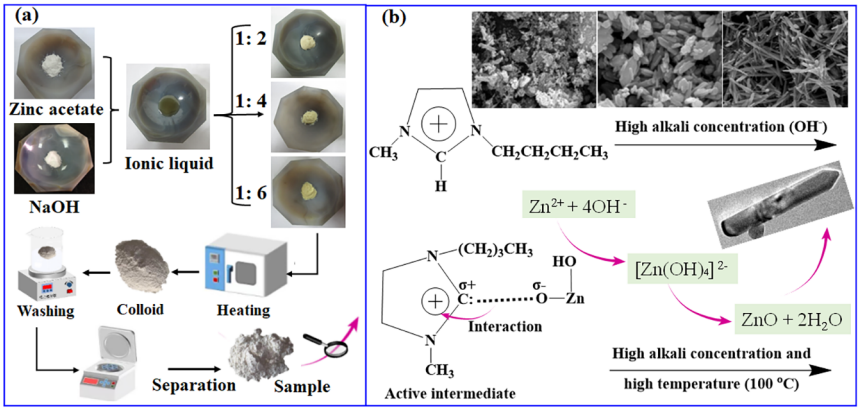


**Figure 2.** (a) Ionic liquid-assisted solid-state synthesis of ZnO photocatalysts in [Bmin]I; (b) schematic diagram of the formation mechanism of ZnO rods in the ionic liquid [Bmin]I at high alkali and temperature.

wonder if other parameters, e.g., alkalinity from the starting materials would influence the structures of ZnO. Thus, smart nanorods obtained at 100 °C with moderate alkalinity ($[Zn^{2+}]/[OH^-]$ as 1:4) were selected as references and parallel experiments of altering alkalinity were attempted. It can be seen from the captured images that irregularly dispersed spherical nanoparticles and a few nanorods were captured with 1:2 molar ratios of $[Zn^{2+}]/[OH^-]$ at 100 °C (sample 4). The sizes of such nanorods were with an average length of about 200−350 nm and an average diameter of about 50−100 nm (Figure 1d). Surprisingly, when the molar ratio of $[Zn^{2+}]/[OH^-]$ was continuously increased to 1:6 and temperature kept the same, the final products are comprised of longer and thinner nanorods with an average length of 3000−5000 nm and a diameter of 300−500 nm (Figure 1e, sample 5). To better understand the nucleation characters and growth mechanisms of regulated structures at relatively higher alkalinity, solid-state synthesis of ZnO without ionic liquid was conducted. Results showed that no significant structures of ZnO were observed under the same conditions, and only irregular nanoparticles were obtained (Figure 1f). These observations suggest that as-employed one-step ionic liquid-based solid-state synthesis using [Bmin]I contributes to the improved crystallinity of ZnO photocatalysts, meanwhile validating the roles of introduced ionic liquid on microstructure manipulations, even at the higher alkalinity and reaction temperature (Table 1). As exhibited in the elemental mappings in Figure 1g−i, sample 3 (prepared at 100 °C, 1:4) not only displays the well-defined individual hexagonal shapes but also acquires higher yields of products that are natured with uniformly distributed/assembled elements.

It can be concluded from the microstructure that when the reaction alkalinity increases from 1:2 to 1:6 at the higher temperature (100 °C), as-obtained products display different growth behaviors from spherical nanoparticles to short nanorods, and further growth to the longer nanorods with exhibiting the increased aspect ratio ($L/D$ = 2 to 10). As observed, the microstructures of ZnO varied from spherical nanoparticles to short nanorods as the temperature increased from 60 to 100 °C, even in the same alkalinity (1:4). Interestingly, the augmented aspect ratios were observed with increasing the reaction temperature, in which the aspect ratio of nanorods is 6.67 times higher than that of $L/D$ exhibited in spherical nanoparticles obtained at the lowest temperature (60 °C). Such structural variations depict that the relatively higher temperature and alkalinity in identical amounted ionic liquid [Bmim]I favor the directional growth of ZnO nanorods with regulated aspect ratios (Figure 2a). It was articulated that physiochemical characteristics of the ionic liquid. e.g., molecular structure, polarity, viscosity, melting/boiling point, and surface tension would play significant roles in the catalyst's nucleation and further growth, subsequently determining their crystal shapes and microstructures.[30,31] Significantly, the polarity, surface tensions, and viscosity are the main influential factors for the material crystallizations in the 1-alkyl-3-methylimidazolium-based ionic liquids, especially with halogen elements ($Cl^-$, $Br^-$, and $I^-$).[31] Herein, [Bmim]I is stable at a higher alkaline environment and reaction temperature (100 °C), which is lower than its decomposing temperature (265 °C). Thus, structural aspects of both ZnO and ionic liquid might be responsible for the directional growth of smart nanorods at 100 °C. Generally, ZnO is composed of several alternating planes of fourfold tetrahedrally coordinated $O_2^-$ and $Zn^{2+}$ stacked alternatively along the $c$-axis. It can be assumed from the structural characters that hydrogen atoms at position 2 (the bond length of C−H is 2.504 Å, Scheme 1) of the imidazole ring react with the negatively charged O−terminated planes of ZnO, resulting in normal dipole moments and spontaneous polarizations along the $c$-axis. As a result, the surface energy of the polar planes is decreased, and the surface charges would be compensated with the introduced ionic liquid. With such decreases in the surface energies, a relatively slow growth rate and exposure of the polar faces are ensured, leading to the preferential growth of the captured nanorods. In


https://doi.org/10.1021/acsami.3c02286
ACS Appl. Mater. Interfaces 2023, 15, 23185−23198

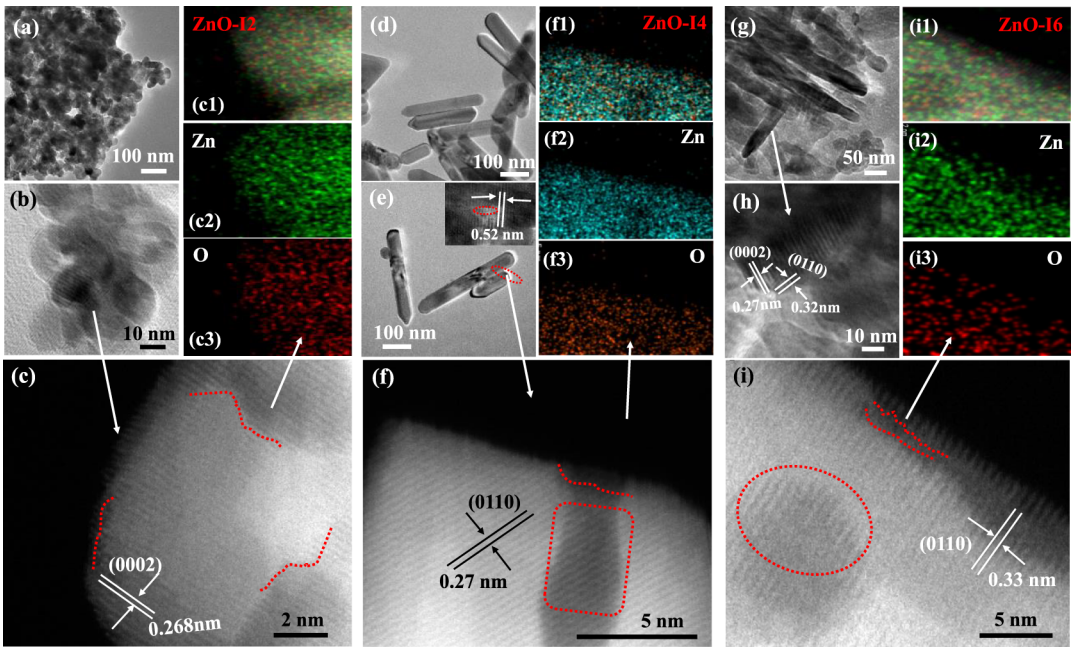


**Figure 3.** (a, b) TEM/HRTEM images, (c) atomic-resolution HAADF-STEM images, and (c1−c3) corresponding elemental mapping of spherical nanoparticles in ZnO-I2; (d, e) TEM/HRTEM images, (f) atomic-resolution HAADF-STEM images, and (f1−f3) corresponding elemental mapping of and short nanorods of ZnO-I4; (g, h) TEM/HRTEM images, (i) atomic-resolution HAADF-STEM images, and (i1−i3) corresponding elemental mapping of and long nanorods of ZnO-I6 photocatalysts, respectively.

other words, the ionic liquid could influence the nucleation of ZnO due to various interactions such as hydrogen bonds, self-assembly, or electrostatic attraction, etc. We assume that the cations of the ionic liquid $[Bmim]^+$ might fully cover the catalyst's surfaces (e.g., ZnO nuclei $Zn(OH)_4^{2-}$) due to the electrostatic attractions during the crystal growth process, and influence the directional assembly of ZnO into the desired structures (the inset in Figure 2b). Therefore, the ionic liquid utilized in this work acts as a green solvent/template to provide the active sites for the nucleation/growth of ZnO. Importantly, higher temperature and alkalinity provide enough reaction speed, promote surface interaction and ion mobility, facilitate nucleation, and result in preferential growth of the nanorods in ZnO. Thus, cooperation of higher temperature and alkalinity within the identical amounted ionic liquid atmosphere play significant roles in nucleation rates and proposal growth of ZnO photocatalysts. Prepared at different alkalinities (1:2, 1:4, and 1:6) at the higher temperature (100 °C), ZnO with well-tuned microstructures are chosen as representatives for the following studies and marked as ZnO-I2, ZnO-I4, and ZnO-I6, respectively.

More structural information of the representative ZnO-I photocatalysts was inspected by HRTEM and an AADF-STEM characterization. Observably, aggregated spherical nanoparticles with size distributions of 20−50 nm are captured in the HRTEM of ZnO-I2, agreeing well with SEM results (Figure 3a,b). The HAADF results exhibited that the crystalline stripes of two lattice spacings in spherical nanoparticles are 0.268 nm corresponding to atomic stacking of (0002) planes, on which the composited elements were uniformly distributed (Figure 3c,c1−c3). Figure 3d,e shows HRTEM profiles of ZnO-I4, in which entire products are comprised of very uniform and overlapped short nanorods with an average length of 300−500 nm and diameter of about 50−100 nm, respectively. With careful observation, it is found that the edges of short nanorods displayed smoother, more transparent, and clear surfaces of the hexagonal crystal, demonstrating well-crystallinity, exposed facets, and orientational growth of ZnO-I4 in ionic liquid (Figure 3e). Interestingly, a few breakages were captured on the hexagonal-shaped short nanorods, suggesting the lattice disorder in the structure. Indeed, HRTEM images for hexagonal short nanorods indicate a disconnection in the marked area (the inset in Figure 3e), though clear crystalline structure with interplanar *d*-spacing of 0.52 nm, which is attributed to the (0001) planes of hexagonal ZnO, indicating preferential growth along the [0001] direction and certain defects on the surface. HAADF observations of single nanorods from ZnO-I4 indicate the obvious atomic structure of short nanorods, the surfaces of which are enriched with the discontinuous arrangement of the atoms (the edge and circled area in Figure 3f), and clear lattice spacing of 0.27 nm. Excitingly, uniform distributions of Zn and O elements and the partially disconnected edges of nanorods can be observed, further suggesting atomic-leveled surface defects in ZnO-I4 (Figure 3f1−f4). Furthermore, long nanorods exhibiting uniform diameters of 20−40 nm are observed in ZnO-I6 and display rough/disordered surfaces (Figure 3g). Meanwhile, the HRTEM of a single nanorod taken from the surface of ZnO-I6 displayed two lateral distances of 0.27 and 0.32 nm, respectively (Figure 3h). These results reveal the directional growth behaviors of the observed single ZnO nanorods in the [0001] orientations, implying the growth direction as [0001] and side planes, e.g., $(10\bar{1}0)$, $(01\bar{1}0)$, $(1\bar{1}00)$, and $(\bar{1}100)$ planes. Detailed microscopic analyses of single nanorods in ZnO-I6 were observed by HAADF, in which the interrupted, disordered edges, and dark frames with lattice spacings of 0.33 nm were captured (Figure 3i). Besides, the elemental mapping analysis proved a relatively uniform elemental distribution of Zn and O (Figure 3i1−i3). We assumed that the unique preparation might promote interaction between ionic liquid


https://doi.org/10.1021/acsami.3c02286
ACS Appl. Mater. Interfaces 2023, 15, 23185−23198

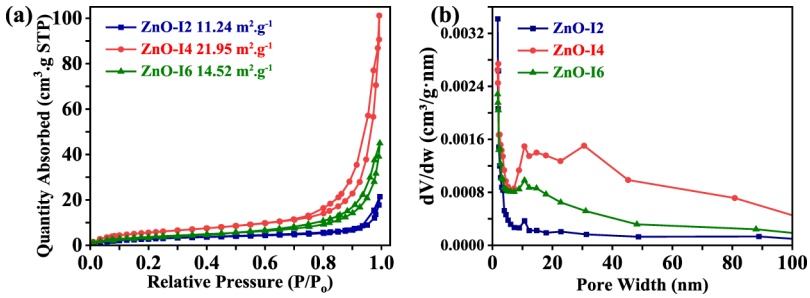


**Figure 4.** (a) BET surface areas and (b) porosity of as-tuned ZnO-I photocatalysts.

and ZnO by influencing nucleation rates and becoming prime reasons for the preferential growth of these smart nanorods. Especially, very significant increases in longitudinal sizes can be observed in ZnO-I2, ZnO-I4, and ZnO-I6, demonstrating the significance of alkalinity in generating diverse microstructures. From the crystallography point of view, the hexagonal ZnO can be described as hexagonal-close-packed O and Zn in its space group $P_6^3mc$ with Zn atoms in tetrahedral sites.[26] The observed (0001) or (000$\bar{1}$) facets of ZnO are the polar facets with Zn or O termination, while (10$\bar{1}$0) are the nonpolar facets. On both O-terminated planes, the electrostatic interaction between the cations of the ionic liquid and the O-terminated surfaces of ZnO may lead to a decrease in the surface energies, generating assorted growth rates and exposing the polar surfaces. It was concluded from the above results that the introduction of ionic liquids plays a significant role in tuning the surface energy of the crystal planes of ZnO. Importantly, the OH is a strong electrolyte that could attract the H atom of position-2 carbon of the imidazole ring of ionic liquid during the proposal synthesis of ZnO at higher alkalinity. In other words, the H-bonding interactions act as important driving forces for self-assembly and support the spontaneous growth of ZnO nanorods toward the [0001] directions. Overall, microstructure diversities in ZnO indicate that alkalinity is beneficial for tuning the ionic interaction between catalyst and ionic liquid [Bmim]I, subsequently varying the electronic forces and growth behaviors to generate as-studied ZnO-I photocatalysts.

It was confirmed from the above analyses that the comparable interactions between the ionic liquid [Bmin]I and starting raw materials must lead to the formation of diverse microstructures and wrinkles in the captured nanoparticles/short nanorods, further indicating their unique surface characteristics, e.g., active reaction sites, surface areas, or porosity. To get more insights into the microstructure-dependent surface-active sites, the physical properties of ZnO-I were investigated by $N_2$ adsorption−desorption isotherms. The BET surface areas are determined as 11.24 $m^2 \cdot g^{-1}$ (ZnO-I2, spherical nanoparticles), 21.95 $m^2 \cdot g^{-1}$ (ZnO-I4, short nanorods), and 14.52 $m^2 \cdot g^{-1}$ (ZnO-I6, long nanorods), respectively (Figure 4a). All the products acquire much higher surface areas than that of reported ZnO crystals, whose BET surface areas were 5.4, 8.4, and 10.5 $m^2 \cdot g^{-1}$, respectively.[32−34] Interestingly, the surface area of ZnO-I4 is larger than its counterparts even prepared at the same reaction temperature, which may be due to the increased interactions and well-manipulated microstructural changes. Moreover, the pore size distributions of as-tuned ZnO-I range from 10 to 30 nm, as depicted in Figure 4b, agreed well with observed trends of surface areas and SEM results. It is interesting to find that the specific surface areas of the as-tuned ZnO-I photocatalysts kept the same trends with their microstructures and aspect ratios, which might devote more adsorption sites for the probe molecules during the photocatalytic reaction. Herein, the employed ionic liquid-assisted synthesis provides a promising and flexible method that can overcome tedious procedures of conventional material preparations, in which microstructure tuning (morphology, active reaction sites, exposed crystal facets, and surface defects) and surface interface controlling of photocatalysts are no longer limited by using templates, shape controlling, or structure-directing agents. Therefore, a moderate, feasible, time-saving, and cost-effective low-temperature solid-state route using green solvent ionic liquid growth techniques on a flexible surface was highlighted in this study.

**3.2. Crystal Structure/Chemical Composition Determination.** As observed in XRD patterns of ZnO, main diffractions at 31.9° (10$\bar{1}$0), 34.6° (0002), 36.5° (10$\bar{1}$1), 47.7° (10$\bar{1}$2), 56.8° (11$\bar{2}$0), and 63.1° (10$\bar{1}$3) were in good agreement with the hexagonal wurtzite phase of ZnO (space group $P_6^3mc$, JCPDS card No. 36-1451, $a$ = 3.2541 Å, $c$ = 5.2038 Å), respectively (Figure 5a). No diffraction peaks from any other impurity phases such as $Zn(OH)_2$ are found in these patterns, validating that the addition of ionic liquids did not change the phase/lattice parameters, but resulted in well-crystallized ZnO photocatalysts. Moreover, (10$\bar{1}$0) and

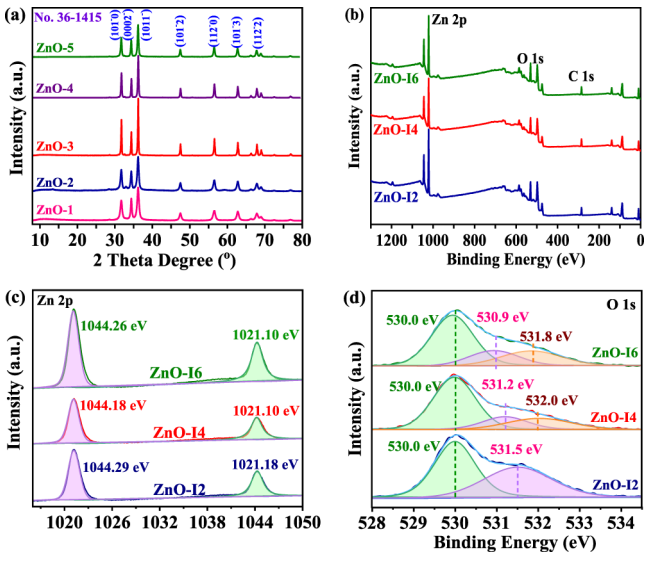


**Figure 5.** (a) XRD patterns of ZnO photocatalysts obtained in ionic liquids; (b) XPS full survey spectra, and (c and d) high-resolution XPS spectra of Zn 2p and O 1s on the surface of as-tuned ZnO-I, respectively.


https://doi.org/10.1021/acsami.3c02286
ACS Appl. Mater. Interfaces 2023, 15, 23185−23198

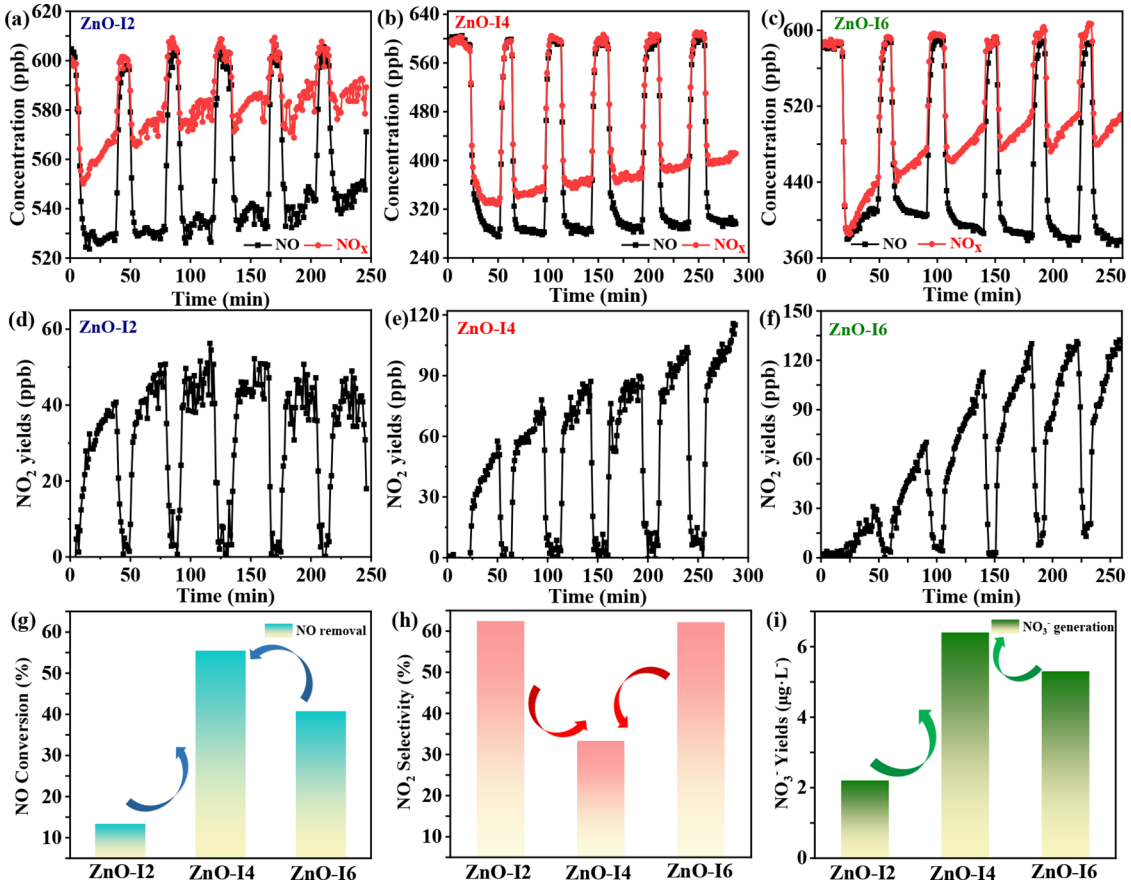


**Figure 6.** Photocatalytic NO conversions in the presence of as-tuned samples: (a–c) inlet/outlet concentrations change of NO and $NO_x$ with long-term light exposure (>250 min); (d–f) $NO_2$ generations during the NO conversion tests; (g and h) comparisons of photocatalytic NO removal efficiency and $NO_2$ selectivity, and (i) final oxidation products $NO_3^-$ generations over as-obtained ZnO-I2, ZnO-I4, and ZnO-I6 photocatalysts, respectively.

(0002$^-$) peaks in the patterns are significantly enhanced among the as-tuned ZnO photocatalysts, indicating their assorted growth behaviors, e.g., preferential growth along certain orientations.

To explore the intrinsic surface chemical states and subsurface components of ZnO-I catalysts, all the elements were measured by XPS. As exhibited in Figure 5b, the full survey spectra indicate the coexistences of composed elements Zn and O on the surfaces, respectively. Indeed, except calibration peaks of C 1s signals at around 284.8 eV, no other impurities from introduced materials or structure-directing agents (e.g., I species) were found, further demonstrating their phase purities (Figure 5b). The Zn 2p spectrum of samples demonstrates doublet at binding energies of 1021.1 and 1044.2 eV, ascribed to the Zn $2p_{3/2}$ and Zn $2p_{1/2}$ states, respectively (Figure 5c).[21] The typical strong peaks located at 530–532 eV in the deconvoluted high-resolution spectrum of O 1s are observed and can be assigned to the $O^{2-}$ species in the crystal lattice ($O_L$), chemisorbed oxygen species caused by surface hydroxyl groups (−OH) and oxygen vacancies ($V_o$), respectively (Figure 5d).[26,35] The decreased peak intensities/areas in 530.0 eV imply the loss of chemisorbed oxygen and accompanying the disappearance of OH in the samples, while slight shifts of the binding energies might result from the coulomb coupling force between $[Bmim]^+$ adsorbed on the surfaces of ZnO, causing the electrons transfer. Such increased electron concentrations of neighboring species, e.g., Zn, and accordingly, lead to a significant decrease of the binding energies both of hydroxyl and adsorbed oxygen. The oxygen defect-related peaks at around 531.2–531.8 eV also displayed significant differences, in which short nanorod-shaped ZnO-I4 demonstrated the larger peak areas, suggesting the existence of surface vacancies. It can be seen from the previous reports that reducing agents or structure-directing agents are helpful for the generations of oxygen defects, concentrations of which increase with the enhancement of annealing temperatures. The oxygen vacant sites broke the electrical neutrality of ZnO, and the nearby $Zn^{2+}$ transformed to $Zn^+$ with the other $e^-$ bound by oxygen vacant sites. In our cases of synthesizing ZnO-I photocatalysts, the passive and reducing atmosphere of ionic liquid under a low temperature might be responsible for the generations of intrinsic defects in the lattice (Figure 5d). Furthermore, the atomic compositions of Zn and O in ZnO-I4 were calculated by using the integrated peak area, and the atomic ratio of Zn:O is 1:0.78, respectively. Such changes in samples might also be related to the microstructures of ZnO-I, whose aspect ratio becomes higher from nanoparticles to short/long nanorods. It is worth mentioning that the existence of surface defects in photocatalysts is beneficial for the trapping of electrons/holes during the reaction and promotes photocatalytic redox reactions upon light illumination.[36–38]

**3.3. Photocatalytic NO Removal Activity.** With such successful microstructure regulations and surface tuning, as-


https://doi.org/10.1021/acsami.3c02286
ACS Appl. Mater. Interfaces 2023, 15, 23185–23198

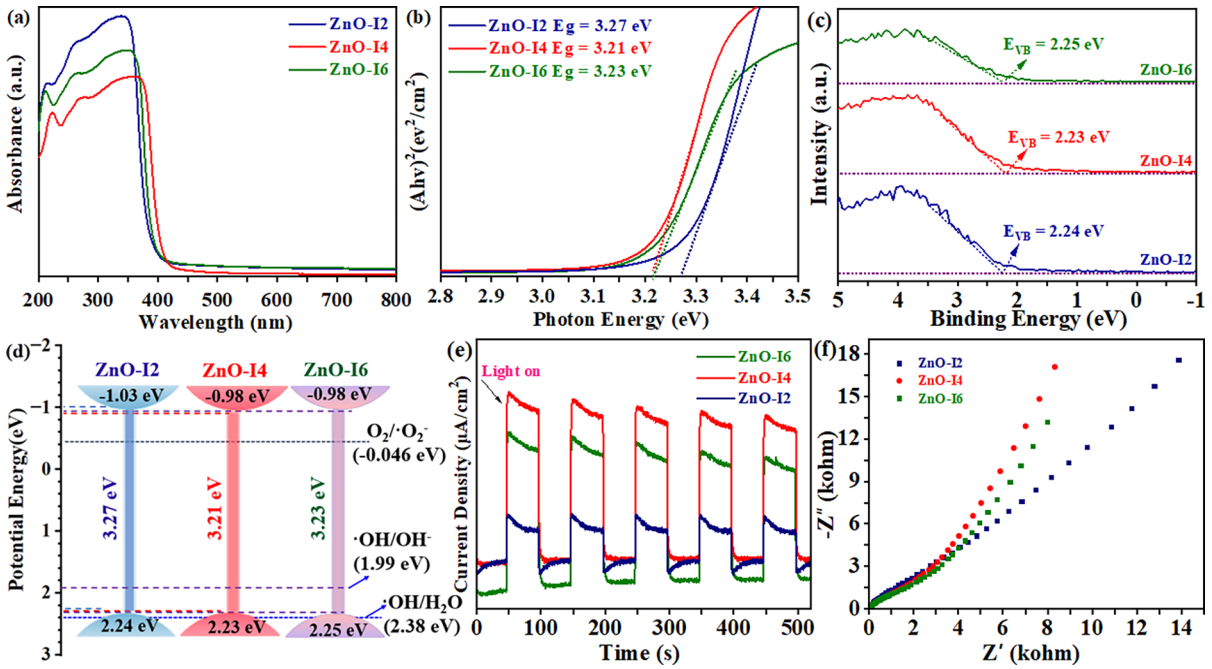


**Figure 7.** (a and b) Room-temperature UV−vis absorption and the corresponding plot of $(\alpha h\nu)^2$ versus photon energy $h\nu$; (c) XPS-VB spectra depicting valence band edge positions of as-tuned ZnO-I samples; (d) energy diagram depicting band edge positions; (e) photocurrent responses; and (f) Nyquist plot of electrochemical impedance spectroscopy of as-obtained ZnO-I2, ZnO-I4, and ZnO-I6 photocatalysts, respectively.

regulated ZnO-I were further employed as potential photocatalysts for the removal of highly toxic, low concentrated (ppb level) potential atmospheric pollutant NO under the simulated light illumination. A series of blank experiments such as NO conversions in the absence of light illumination and catalyst powders were attempted (Figure S1, in the SI). Control tests indicated no obvious decrease in NO levels without ZnO samples and direct light irradiation. After the blank tests, optimum conditions were determined, under which the results suggested that the NO concentration decreased to a certain extent upon prolonging irritation time. The NO removal efficiency is defined as $C_{NO,out}/C_{NO,in}$, where $C_{NO,in}$ and $C_{NO,out}$ are the inlet and outlet concentration of NO (~ppb) before and after the reaction, respectively. It was indicated that all representative ZnO-I catalysts display certain photocatalytic NO removal and $NO_2$ intermediate formation. After 250 min long period irradiation of solar light, NO concentrations are drastically decreased in the presence of as-tuned ZnO-I, and final conversion efficiencies of NO were: ZnO-I4 (55.45%) > ZnO-I6 (40.74%) > ZnO-I2 (13.33%), respectively (Figure 6a−c). As observed, the highest NO removal efficiency (55.45%) was observed in short nanorod-shaped crystals (ZnO-I4), nearly 4.15 and 1.36 magnitude order higher than its counterparts, spherical nanoparticles (ZnO-I2) and long nanorods (ZnO-I6), respectively (Figure 6g). Moreover, NO concentrations in such a system incline to keep a stable decrease even after six cycles with a longer than 250 min irradiation period, suggesting robust stability and higher efficiency of ZnO. This can also be evidenced by the unchanged crystal structures evaluated by XRD characterizations after the six runs of NO conversion tests (Figure S2, in the SI), further indicating that as-tuned photocatalysts are stable and qualified to be used in practical applications. Note that the NO removal is a typical solid−gas reaction, in which ZnO photocatalysts are immobilized in the solid phase to avoid any photocorruption, meanwhile underlining their further advantages in the field of air pollution control. Significantly, the intermediate generations and their concentrations during the photocatalytic NO conversions should be considered carefully, especially during such a long irradiating interval. Considering the higher toxicity of the extremely undesirable intermediate $NO_2$ than NO itself, the accurate concentration changes of $NO_2$ were analyzed with the concentration differences of NO and $NO_x$ at the given interval. It is worth noticing that after 250 min light irradiation, the concentrations of $NO_2$ over ZnO-I2 display steady values (41−50 ppb), while outlet values of $NO_2$ gradually increased from 56 ppb at 50 min to 109 ppb at 250 min in ZnO-I4, respectively (Figure 6d,e). Astonishingly, the highest outlet concentration of $NO_2$ was observed in the presence of ZnO-I6, in which the $NO_2$ concentration was steadily increased to 114 ppb at 140 min and kept stable at 131 ppb with prolonging the irradiation time till 300 min (Figure 6f). Overall, after long-term (250 min) light illumination, the outlet concentrations of toxic intermediate $NO_2$ over as-tuned ZnO-I were 50 ppb (ZnO-I2) < 110 ppb (ZnO-I4) < 140 ppb (ZnO-I6), respectively. Correspondingly, $NO_2$ selectively over studied samples are estimated, and an optimal $NO_2$ selectivity was found in a short nanorod-shaped ZnO-I4 crystal with a selectivity of 33.33%, which was much ideal than that of $NO_2$ selectivity produced over its counterparts ZnO-I6 (62.22%) and ZnO-I2 (62.51%), respectively (Figure 6h). To evaluate accurate conversion products of NO, the concentrations of oxidation species $NO_3^-$ were determined by ion chromatography via analyzing the washing solution of the samples used for the NO removal test. The $NO_3^-$ concentrations over as-tuned samples were 2.2, 6.4, and 5.3 $\mu g \cdot L^{-1}$, respectively (Figure 6i). The detected $NO_2$ and $NO_3^-$ over samples were consistent with the consumed NO in the system, indicating that these were the main NO conversion products over ZnO photocatalysts. As evidenced by $NO_2$ suppression and $NO_3$ production during the NO removal, successful microstructure regulations of ZnO promote selective NO oxidation and


https://doi.org/10.1021/acsami.3c02286
ACS Appl. Mater. Interfaces 2023, 15, 23185−23198

Table 2. Microstructural, Optical Properties, and NO Removal Performances of ZnO-I Photocatalysts

| | | | band edge positions (eV) | | NO conversion | | |
|---|---|---|---|---|---|---|---|
| samples | BET ($m^2 \cdot g^{-1}$) | band gap (eV) | valence band | conduction band | $\eta$ (%) | $NO_2$ (ppb) | $S_{NO_2}$ (%) |
| ZnO-I2 | 11.24 | 3.27 | 2.24 | −1.03 | 13.33 | 50 | 62.51 |
| ZnO-I4 | 21.95 | 3.21 | 2.23 | −0.98 | 55.45 | 110 | 33.33 |
| ZnO-I6 | 14.52 | 3.23 | 2.25 | −0.98 | 40.76 | 131 | 62.22 |

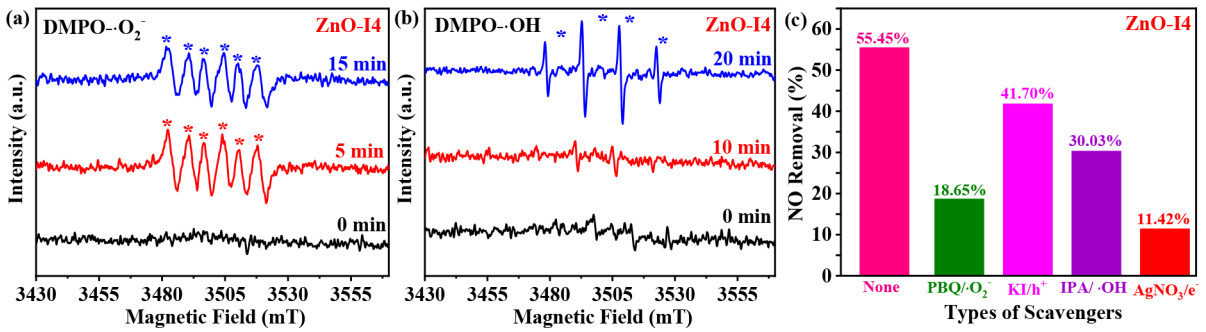


Figure 8. (a and b) ESR detection of active species (·OH and $\cdot O_2^-$) using a DMPO spin−trapping agent; (c) active radical detection with assorted scavengers over ZnO-I4 photocatalysts, respectively.

impact on their effectiveness for intermediate control. Furthermore, these results turn out to be more appreciable when compared with the state-of-the ZnO-based photocatalysts for NO removal (Table S1, in the SI).

**3.4. Investigations of Photocatalytic Mechanism and Structure−Performance Correlations.** To reveal the impact of microstructures on the optical absorptions of as-tuned ZnO-I photocatalysts, the UV−vis diffuse reflectance spectroscopy (DRS) tests were carried out. As depicted in the absorption profiles, ZnO-I displayed very little differences in the absorption at wavelengths shorter than 400 nm, which can be assigned to the intrinsic band gap absorption of ZnO due to the electron transitions from the valence band to the conduction band (O 2p → Zn 3d, Figure 7). Significantly, the broadened and enhanced absorptions in the UV region are observed in ZnO-I, suggesting a higher degree of crystallinity and well-defined microstructures. The absorption onsets of ZnO-I samples are estimated to be 379 (ZnO-I2), 386 (ZnO-I4), and 383 nm (ZnO-I6), respectively (Figure 7a). The shift of absorption edges toward longer wavelengths with increasing the size of ZnO indicates the decrease in their band energies. It was demonstrated that such absorption shifts might also be related to the formation of shallow electronic states inside the band gap because of intrinsic defects in the lattice.[39] The HAADF-STEM (Figure 3) and XPS-O 1s profiles (Figure 5d) indicate the presence of such surface oxygen defects on the surface of as-obtained ZnO-I photocatalysts. Empirically, the Kubelka−Munk function was employed to determine accurate band gaps of ZnO-I photocatalysts:

$$\alpha h\nu = A(h\nu - E_g)^{n/2}$$

where $\alpha$, $\nu$, $A$, and $E_g$ are the absorption coefficient, incident light frequency, constant, and band gap, respectively.[40] Based on the direct transition characters of the ZnO catalyst, the $E_g$ values of as-tuned samples were calculated from the linear intersection, while $(\alpha h\nu)^2$ was plotted versus energy $h\nu$. Accordingly, corresponding band gaps of samples are estimated to be 3.27 (ZnO-I2), 3.21 (ZnO-I4), and 3.23 eV (ZnO-I6), respectively (Figure 7b). The narrower band gaps are beneficial for charger carrier generations, and enhance photocatalytic effectiveness, validating the reasons for enhanced NO removal over ZnO-I4 catalyst than its counterparts. Corresponding band edge positions of ZnO-I photocatalysts were analyzed since band structures of semiconductors not only affect the redox ability but also determine photocatalytic activity. Herein, to investigate the impact of microstructures on the band energy structure, including estimating the accurate valence band (VB) positions of as-tuned ZnO-I photocatalysts, the XPS-VB spectra were employed. As depicted in Figure 7c, the VB values of ZnO-I photocatalysts were determined to be 2.24 (ZnO-I2), 2.23 (ZnO-I4), and 2.25 eV (ZnO-I6), respectively. Meanwhile, conduction band (CB) positions of samples were calculated from $E_{CB} = E_{VB} - E_g$, and followed the order of −1.03 (ZnO-I2), −0.98 (ZnO-I4), and −0.98 eV (ZnO-I6), respectively.[41,42] Note that the CB positions of ZnO-I are much higher than that of redox potentials of superoxide radicals ($E(O_2/\cdot O_2^-)$ = −0.046 eV vs NHE, pH = 7.0) formations, indicating greater active species, e.g., superoxide radicals ($\cdot O_2^-$) production upon light irradiations (Figure 7d).[42] Effective generations of active species can treat atmospheric pollutants by improved redox reactions, which have been accepted as an efficient strategy for the removal of NO with low concentration from the air. On the other hand, with unique microstructures and optical characters, the separation efficiency of the charge carrier might be enhanced, which was supported by electrochemical measurements. As exhibited in Figure 7e, the photocurrent responses of as-regulated samples are different, in which ZnO-I4 and ZnO-I6 acquire higher photogenerated electron transfer rates, implying that the photogenerated carriers in these samples would be easier to separate and devote improved photocatalytic activities. The interface charge separation efficiency of photogenerated electrons and holes was further investigated by the typical EIS. The arc radius of ZnO-I4 is larger than its counterparts, suggesting that microstructure regulation on ZnO can dramatically increase the efficiency of charge carrier separation and transformations (Figure 7f). Hence, the regulated microstructures and optical characters of as-tuned samples can be regarded as the main significant factors that are


https://doi.org/10.1021/acsami.3c02286
ACS Appl. Mater. Interfaces 2023, 15, 23185−23198

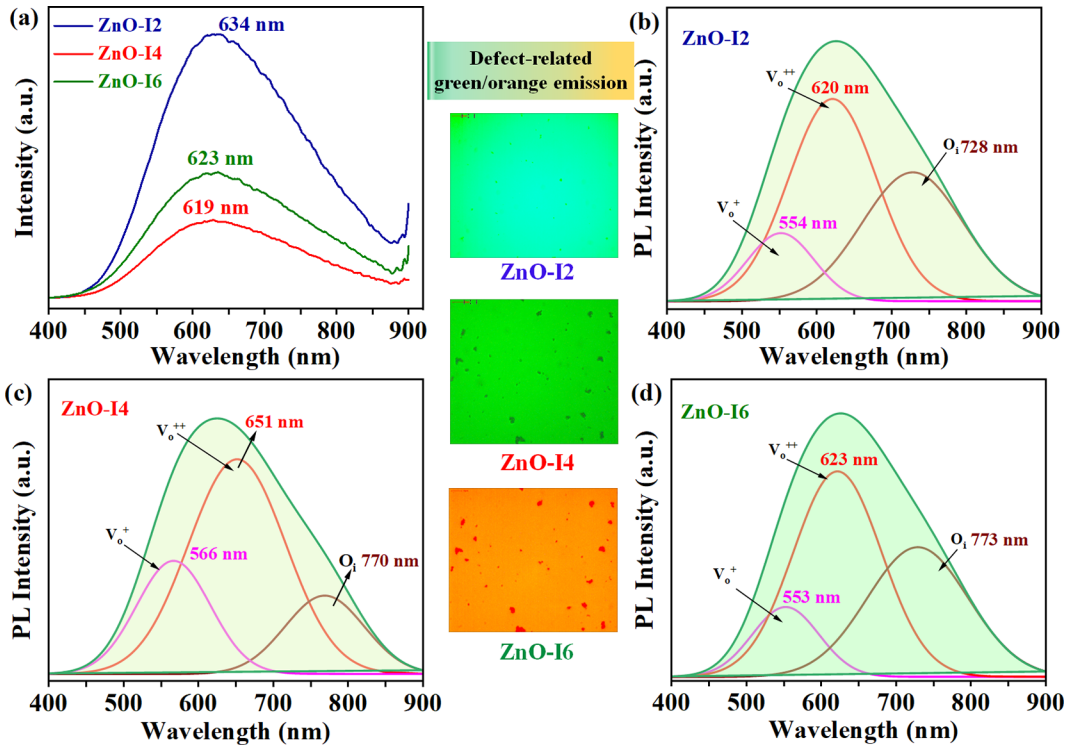


**Figure 9.** (a) Room-temperature photoluminescence spectra and images and (b–d) Gaussian fits of each PL spectrum of as-obtained ZnO-I2, ZnO-I4, and ZnO-I6 photocatalysts, respectively.

contributing to the improved photocatalytic NO removal, especially in the ZnO-I4 photocatalyst. The microstructural, optical properties, band edge positions, and NO removal performances of representative ZnO-I photocatalysts are summarized in Table 2.

To prove the above assumption and inspect the involved active species in the NO removal tests, the semi-situ ESR measurements with 5,5-dimethyl-a-pyrroline *N*-oxide (DMPO) as a spin-trapping agent were conducted.[43−45] As exhibited in Figure 8a, no obvious ESR peaks were observed in the absence of light illuminations in both representative $\cdot O_2^-$ and ·OH signal lines. After 5 min light illumination, six characteristic ESR signals with equal peak intensity ratio were captured and can be attributed to $\cdot O_2^-$ produced in ZnO-I4. The captured ESR signals from DMPO-$\cdot O_2^-$ get enhanced with 15 min further light irradiation, indicating that the $\cdot O_2^-$ is the main species contributing to NO removal (Figure 8a). Comparably, no significant ESR signals from DMPO-·OH were detected in ZnO-I4, even after 10 min light illumination. When the samples were further explored to 20 min light illumination, significant four-wire ESR signals with the intensity of 1:2:2:1 representing ·OH radical were captured, which suggest that there was a certain amount of ·OH radicals generated from the reactions of adsorbed $OH^-$ by photoinduced $h^+$ on the surface of ZnO-I4 (Figure 8b). The quantitative results of the involved active species over as-tuned ZnO-I4 photocatalysts were investigated by a series of scavenger tests. Typically, *tert*-butyl alcohol (TBA) was used as an ·OH scavenger, potassium iodide (KI) as an $h^+$ hunter, *p*-benzoquinone (PBQ) for quenching $\cdot O_2^-$ and potassium dichromate ($K_2Cr_2O_7$) as an $e^-$ trapper, respectively.[24] As exhibited in Figure 8c, the NO conversion is partially achieved when the KI is added into the system, demonstrating that $h^+$ is not the major radical but exerts certain roles for photocatalytic NO removal. The $NO_2$ formations in ZnO-I4 photocatalysts might be the roles due to the $h^+$ since their strong oxidation capabilities of the $h^+$ on the surfaces of the samples. When TBA was added as ·OH radical hunter into the reaction, the NO removal was partially restricted, disclosing that ·OH holds a minor role but is not the influencing factor for the reaction in representative ZnO-I4 photocatalysts. It is acceptable since the VB positions of ZnO-I catalysts did not meet the requirements for boosted generations of the ·OH species ($\cdot OH/H_2O$ = 2.38 eV vs NHE, pH = 7.0), especially for such gas−solid reactions. Compared with NO removal without any trapping agent, the outlet concentration of NO is obviously suppressed after adding PBQ and $K_2Cr_2O_7$ as $\cdot O_2^-$ and $e^-$ hunters, demonstrating that these species are the important ones that contribute to the promoted NO removal. Many advanced oxidation processes for NO removal are mainly related to such essential radicals, the presence of which could enhance NO selectivity and achieve completed oxidation into $NO_3^-$ species.[7,8,46] It is predicted in this case that the suitable conduction band edge positions of ZnO-I photocatalysts could achieve the molecular oxygen activation via the reaction of photoinduced electrons and surface-adsorbed oxygen ($O_2 + e^- = \cdot O_2^-$), and lead to successful oxidation of dilute NO. Improved NO removal through boosted $O_2$ production and strengthened surface interactions were also verified in our recent work from both experimental and theoretical aspects.[24]

Effective separation and enhanced transfer of photoinduced charge carriers are two competing reaction pathways and the most important determinantal approaches to enhance the NO removal performances of photocatalysts. Herein, room-temperature PL spectra of as-regulated ZnO-I were analyzed to inspect the charge carrier separations as PL emission was induced from the exciton recombination or intrinsic defects. The excitation wavelength was determined as 325 nm, and


https://doi.org/10.1021/acsami.3c02286
ACS Appl. Mater. Interfaces 2023, 15, 23185−23198

corresponding PL intensities over samples were ZnO-I2 > ZnO-I6 > ZnO-I4, respectively (Figure 9a). Strong and broad emissions observed at 619−634 nm in samples come from oxygen interstitial atoms, which indicates that as-tuned ZnO-I photocatalysts exhibit prominently visible emissions. As observed, the luminescence intensity of ZnO-I4 exhibits an obvious decrease, which implies the longer lifetime of its photoinduced electrons and holes. With the lowest emission, ZnO-I4 displayed the most pronounced defect-related emission, suggesting suppressed charge carrier recombination. Observed green and red-orange emissions in samples are commonly assigned to the deep surface defects levels, e.g., oxygen and Zn vacancies in ZnO.[47−49] It can be observed from the results that the luminescence emission peak position remains unchanged with an increase in the crystal size in as-tuned ZnO. Interestingly, representative samples display green-orange emissions when they were subjected to fluorescence microscope observations (Figure 9a, below). It is worth pointing out that the surfaces of ZnO catalysts are fully covered/adsorbed by ionic liquid during such low-temperature synthesis and treated with simple washing without further calculations. Hence, as-tuned ZnO would exhibit unsaturated surfaces with daggling $O_2^-$, deprivation of which is beneficial for the surface defect constructions. We assumed that these surface defects in ZnO are the prime reasons for the observed emissions. However, the origins of the broad emissions are still controversial, and always explained based on assorted charge states, surface defects and vacant sites (zinc vacancies and zinc interstitial) in the structure. To get a deeper understanding of the light emissions in as-tuned ZnO, the emission peaks were analyzed by the peak fitting method. It can be observed from the results that PL emissions in all samples display three peaks (Figure 9b−d). The green emission peaks at around 553−566 nm are attributed to the recombination of electrons trapped in singly ionized oxygen vacancies ($V_o^+$) with photogenerated holes.[33,50] The broad emissions at around 620−650 nm are associated with the doubly ionized oxygen vacancy ($V_o^{+2}$), while orange emissions captured at 720−773 nm are related to the oxygen interstitials ($O_i$), respectively. It was observed from Table 3 that the proportions of defect-related emissions in as-tuned samples are quite different, in which ZnO-I4 displays less $V_o^+$ and relatively higher $V_o^{+2}$ than other counterparts. We assumed that relatively higher proportions of $V_o^{+2}$ in ZnO-I4 could become a superb site to confine surface-adsorbed $O_2$ toward efficient and selective NO oxidation to nitrate. The same observations were demonstrated in the defective BiOCl catalysts, which displayed NO oxidation selectivity from $NO_2$ to $NO_3^-$ with high efficiency.[51] Herein, observed oxygen defects on the surfaces of as-tuned ZnO-I photocatalysts were also optimal to produce the strong oxidant $\cdot O_2^-$, and subsequent improvements of complete NO removal over ZnO-I photocatalysts. Hence, the enhanced NO conversions and successful inhabitations of $NO_2$ over as-tuned ZnO photocatalysts might be attributed to the high-abundant surface defects (oxygen vacancies, zinc interstitials), electron transfer between donor states and NO, which was proved in our recent study.[24]

**Table 3. Distributions of Assorted Species on the Surfaces of Samples**

| samples | $V_o^{++}$ | $V_o^+$ | $O_i$ |
|---|---|---|---|
| ZnO-I2 | 50.42% | 36.79% | 12.78% |
| ZnO-I4 | 58.97% | 17.42% | 23.61% |
| ZnO-I6 | 12.98% | 50.63% | 36.38% |

It can be speculated from the results that the well define microstructures of as-tuned ZnO photocatalysts displayed significant impacts on their optical character, especially on their band edge positions. Therefore, when the light is illuminated on the surfaces of the as-regulated samples, the electrons would transit from their VB to the CB, allowing the effective formation of the charge carriers. These species would further react with the adsorbed $O_2$ and $H_2O$ on the surface of the photocatalysts, resulting in photocatalytically active species $\cdot O_2^-$ and ·OH, respectively. Moreover, the captured ESR results suggested that the boosted $\cdot O_2^-$ radicals production resulted in the enhanced redox reactions due to the surface reaction, e.g., molecular oxygen activations of surface-adsorbed $O_2$ and photoinduced electrons since CB potentials of ZnO-I are more sufficiently negative to produce $\cdot O_2^-$ radicals ($O_2 + e^- = \cdot O_2^-$).[52] Thermodynamically, oxidation product $NO_3^-$ can be achieved in ZnO-I samples due to the reasonable potentials ($NO/NO_3^-$ = 0.94 eV vs NHE, pH = 7.0), quite consistent with the obtained results of $NO_3^-$ formation.[53] On the other hand, the surface defects of ZnO-I are beneficial for the massive production of active species, quench photoinduced electrons, and result in appreciable carrier separations to minimize the radiative recombination of photoinduced charge carriers. Importantly, the built-in electric field-induced excitation leaves holes in VB of ZnO-I, whose VB is more positive than ($\cdot OH/OH^-$ = 1.99 eV vs NHE, pH = 7.0), and generates more ·OH radicals, facilitating NO conversions. It is worth mentioning that the more toxic intermediate $NO_2$ generations over as-investigated samples are mainly associated with the presence of ·OH radicals, formations of which are limited in ZnO-I photocatalysts due to the undesirable

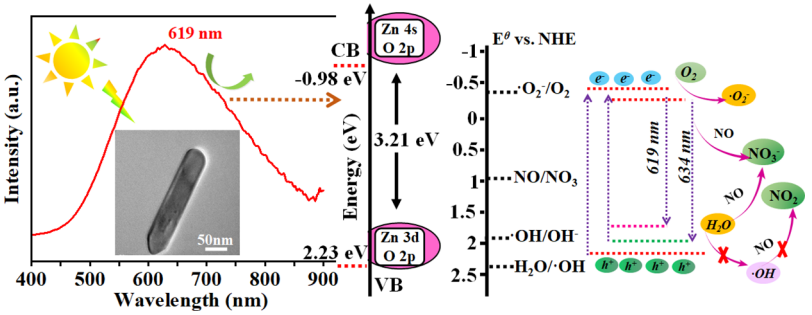


**Figure 10.** Defect-related charge carrier separation and band edge positions of as-tuned ZnO-I4 photocatalyst relative to the energy levels of various redox couples.



https://doi.org/10.1021/acsami.3c02286
ACS Appl. Mater. Interfaces 2023, 15, 23185−23198

thermodynamics (·OH/$H_2O$ = 2.38 eV vs NHE, pH = 7.0). It can be concluded from the above analyses that the enhanced NO conversions and suppressed $NO_2$ generations over as-tuned ZnO-I4 microstructures were assigned to the unique light absorption, effective productions of active species from the well-positioned band edges, and defect-induced carrier separations. Based on the above analyses, a possible reaction mechanism was proposed as shown in Figure 10.

## 4. CONCLUSIONS

In summary, successful microstructure regulations in ZnO were achieved in ionic liquid 1-ethyl-3-methylimidazolium iodide ([Bmim]I)-based solid-state synthesis. By investigating the influences of reaction temperature and alkalinity on the microstructures, nanosphere, short and long nanorod-shaped ZnO with orientated growth behavior were observed, and the formation mechanism of the assorted shapes of ZnO photocatalysts which are based on the self-assembly behavior of ionic liquid was elucidated. Furthermore, NO removal tests were conducted to inspect the influences of microstructures on the photocatalytic activities of as-tuned ZnO. Results showed that successful microstructure regulations in ZnO photocatalysts could largely improve the photocatalytic NO conversions (55.45%) and inhibit the formation of toxic intermediate ($NO_2$) with enhanced reaction selectivity (33%), respectively. Significantly, as-tuned ZnO photocatalysts obtained at optimal conditions displayed defect-related light emission and promoted charge carrier separations. The origins of the enhanced NO removal, improved reaction selectivity and decreased $NO_2$ generation over as-tuned ZnO photocatalysts were further investigated based on the unique crystal structures, microstructure diversity, active radical trapping tests and surface interface characters. Results showed that well-positioned band edges, defect-associated carrier separations, and strengthened surface−interface reaction from active species, etc. contributed to the improved NO removal and remarkably suppressed $NO_2$ generations. We hope, this simple tuning approach can provide instructive information on exploring the intriguing purposive microstructure regulations of environmental photocatalysts and will, in turn, deepen the understanding of the intriguing surface chemistry of photocatalytic NO removal and motivate the practical implementations of cost-effective, highly efficient NO removal systems in the field of environmental pollution control.

## ■ ASSOCIATED CONTENT

### Supporting Information

The Supporting Information is available free of charge at https://pubs.acs.org/doi/10.1021/acsami.3c02286.

Experimental section; control experiments for photocatalytic NO removal tests (Figure S1); Comparative XRD profiles of ZnO-I before and after the NO conversion tests (Figure S2); Comparisons of the state-of-the-art of reported ZnO-based catalysts for photocatalytic NO conversions (Table S1) (PDF)

## ■ AUTHOR INFORMATION


### Corresponding Authors

**Reshalaiti Hailili** − *MOE Key Laboratory of Enhanced Heat Transfer and Energy Conservation, Beijing Key Laboratory of Heat Transfer and Energy Conversion, Beijing University of Technology, Beijing 100124, P. R. China; Institut für Technische Chemie, Gottfried Wilhelm Leibniz Universität Hannover, 30167 Hannover, Germany;* orcid.org/0000-0002-8212-8635; Email: Reshalaiti100@163.com

**Detlef W. Bahnemann** − *Institut für Technische Chemie, Gottfried Wilhelm Leibniz Universität Hannover, 30167 Hannover, Germany; Laboratory "Photoactive Nanocomposite Materials", Saint Petersburg State University, Saint-Petersburg 198504, Russia;* orcid.org/0000-0001-6064-6653; Email: bahnemann@iftc.uni-hannover.de

### Authors

**Xiaokaiti Reyimu** − *MOE Key Laboratory of Enhanced Heat Transfer and Energy Conservation, Beijing Key Laboratory of Heat Transfer and Energy Conversion, Beijing University of Technology, Beijing 100124, P. R. China*

**Zelong Li** − *MOE Key Laboratory of Enhanced Heat Transfer and Energy Conservation, Beijing Key Laboratory of Heat Transfer and Energy Conversion, Beijing University of Technology, Beijing 100124, P. R. China*

**Xu Lu** − *MOE Key Laboratory of Enhanced Heat Transfer and Energy Conservation, Beijing Key Laboratory of Heat Transfer and Energy Conversion, Beijing University of Technology, Beijing 100124, P. R. China*

Complete contact information is available at: https://pubs.acs.org/10.1021/acsami.3c02286


### Author Contributions

All authors have given approval to the final version of the manuscript.

### Notes

The authors declare no competing financial interest.

## ■ ACKNOWLEDGMENTS

Financial support by the National Natural Science Foundation of China (No. 21902161) and the *Alexander von Humboldt* Foundation of Germany is gratefully appreciated. D.W.B. acknowledges financial support from Saint Petersburg State University (Research Grant 39054581). X. Reyimu is a volunteer researcher in R. Hailili's lab.

## ■ REFERENCES


(1) Eurostat. *Air Pollution Statistics-emission Inventories*. https://ec.europa.eu/eurostat/statistics-explained/index.php?title=Air_pollution_statistics_-_emission_inventories&oldid=394947#General_overview (accessed July 1, 2022).

(2) Kim, C. H.; Qi, G.; Dahlberg, K.; Li, W. Strontium-doped Perovskites Rival Platinum Catalysts for Treating $NO_x$ in Simulated Diesel Exhaust. *Science* **2010**, *327*, 1624−1627.

(3) Air Quality Guidelines for Europe. *Copenhagen, World Health Organization Regional Office for Europe*; WHO regional publications, European series, NO. 91, 2000.

(4) Zhu, H. Z. Z.; Nie, G.; Hu, Y. F.; Wang, J. Y.; Bai, H. C.; Li, Y. H.; Guo, Q. J.; Wang, C. P. Experimental Study on Denitration Performance of Iron Complex-based Absorption Solutions and their Regeneration by Zn. *Energy Fuels* **2019**, *33*, 8998−9003.

(5) Han, L. P.; Cai, S. X.; Gao, M.; Hasegawa, J.-Y.; Wang, P. L.; Zhang, J. P.; Shi, L. Y.; Zhang, D. S. Selective Catalytic Reduction of $NO_x$ with $NH_3$ by Using Novel Catalysts: State of the Art and Future Prospects. *Chem. Rev.* **2019**, *119*, 10916−10976.

(6) He, G. Z.; Lian, Z. H.; Yu, Y. B.; Yang, Y.; Liu, K.; Shi, X. Y.; Yan, Z. D.; Shan, W. P.; He, H. Polymeric Vanadyl Species Determine the Low-temperature Activity of V-based Catalysts for the SCR of $NO_x$ with $NH_3$. *Sci. Adv.* **2018**, *4*, No. eaau4637.

(7) Wu, Q. P.; Van de Krol, R. Selective Photoreduction of Nitric Oxide to Nitrogen by Nanostructured $TiO_2$ Photocatalysts: Role of

Oxygen Vacancies and Iron Dopant. *J. Am. Chem. Soc.* **2012**, *134*, 9369−9375.
(8) Xie, S. H.; Tan, W.; Li, Y. J.; Ma, L.; Ehrlich, S. N.; Deng, J. G.; Xu, P.; Gao, F.; Dong, L.; Liu, F. D. Copper Single Atom-Triggered Niobia−Ceria Catalyst for Efficient Low-Temperature Reduction of Nitrogen Oxides. *ACS Catal.* **2022**, *12*, 2441−2453.
(9) Li, N.; Wang, C. Y.; Zhang, K.; Lv, H. Q.; Yuan, M. Z.; Bahnemann, D. W. Progress and Prospects of Photocatalytic Conversion of Low-concentration NOx. *Chin. J. Catal.* **2022**, *43*, 2363−2387.
(10) Rhimi, B.; Padervand, M.; Jouini, H.; Ghasemi, S.; Bahnemann, D. W.; Wang, C. Y. Recent Progress in NOx Photocatalytic Removal: Surface/interface Engineering and Mechanistic Understanding. *J. Environ. Chem. Eng.* **2022**, *10*, No. 108566.
(11) Li, H.; Zhu, H. J.; Shi, Y. B.; Shang, H.; Zhang, L. Z.; Wang, J. Vacancy-Rich and Porous NiFe-Layered Double Hydroxide Ultrathin Nanosheets for Efficient Photocatalytic NO Oxidation and Storage. *Environ. Sci. Technol.* **2022**, *56*, 1771−1779.
(12) Hailili, R.; Wang, Z.-Q.; Ji, H. W.; Chen, C. C.; Gong, X.-Q.; Sheng, H.; Zhao, J. C. Mechanistic Insights into Photocatalytic Reduction of Nitric Oxide to Nitrogen on Oxygen-deficient Quasi-two-dimensional Bismuth-based Perovskite. *Environ. Sci.: Nano.* **2022**, *9*, 1453−1465.
(13) Shi, A. B.; Yang, Z. P.; Shi, L. J.; Li, H.; Liu, X. P.; Zhang, X.; Cheng, J. D.; Liang, C.; Cao, S. Y.; Guo, F. R.; Liu, X.; Ai, Z. H.; Zhang, L. Z. Surface Boronizing Can Weaken the Excitonic Effects of BiOBr Nanosheets for Efficient $O_2$ Activation and Selective NO Oxidation under Visible Light Irradiation. *Environ. Sci. Technol.* **2022**, *56*, 14478−14486.
(14) Zhang, W.; Zhao, J.; Allam, A. A.; Xin, Y.; Lin, J. Q.; Gao, T.; Ajarem, J. S.; Li, X. M.; Wang, C. Y.; Bahnemann, D. W. Palladium Nanoparticles Embedded Nutshell-like $Bi_2WO_6$ as an Efficient and Stable Visible-Light-Responsive Photocatalysts for NO Removal. *Energy Fuels* **2022**, *36*, 13852−13862.
(15) Bahnemann, D. W.; Kormann, C.; Hoffmann, M. R. Preparation and Characterization of Quantum Size Zinc Oxide: A Detailed Spectroscopic Study. *J. Phys. Chem.* **1987**, *91*, 3789−3798.
(16) Wang, J.; Xia, Y.; Dong, Y.; Chen, R. S.; Xiang, L.; Komarneni, S. Defect-rich ZnO Nanosheets of High Surface Area as An Efficient Visible-light Photocatalyst. *Appl. Catal., B* **2016**, *192*, 8−16.
(17) Kansal, S. K.; Ali, A. H.; Kapoor, S.; Bahnemann, D. W. Synthesis of Flower like Zinc Oxide Nanostructure and its Application as A Photocatalyst. *Sep. Purif. Technol.* **2011**, *80*, 125−130.
(18) Bloh, J. Z.; Dillert, R.; Bahnemann, D. W. Transition Metal-modified Zinc Oxides for UV and Visible Light Photocatalysis. *Environ. Sci. Pollut. Res.* **2012**, *19*, 3688−3695.
(19) Barhoum, A.; Melcher, J.; Assche, G. V.; Rahier, H.; Bechelany, M.; Fleisch, M.; Bahnemann, D. W. Synthesis, Growth Mechanism, and Photocatalytic Activity of Zinc Oxide Nanostructures: Porous Microparticles Versus Nonporous Nanoparticles. *J. Mater. Sci.* **2017**, *52*, 2746−2762.
(20) Huang, P.-S.; Qin, F.; Lee, J.-K. Role of the Interface between Ag and ZnO in the Electric Conductivity of Ag Nanoparticle-Embedded ZnO. *ACS Appl. Mater. Interfaces* **2020**, *12*, 4715−4721.
(21) Hegazy, I.; Geioushy, R.; El-Sheikh, S.; Shawky, A.; El-Sherbiny, S.; Kandil, A.-H. T. Influence of Oxygen Vacancies on the Performance of ZnO Nanoparticles towards $CO_2$ Photoreduction in Different Aqueous Solutions. *J. Environ. Chem. Eng.* **2020**, *8*, No. 103887.
(22) Li, P.; Hu, H. F.; Luo, G.; Zhu, S.; Guo, L. J.; Qu, P.; Shen, Q.; He, T. Crystal Facet-dependent $CO_2$ Photoreduction over Porous ZnO Nanocatalysts. *ACS Appl. Mater. Interfaces* **2020**, *12*, 56039−56048.
(23) Zhao, Y. Y.; Liu, N. S.; Zhou, S.; Zhao, J. J. Two-dimensional ZnO for the Selective Photoreduction of $CO_2$. *J. Mater. Chem. A* **2019**, *7*, 16294−16303.
(24) Hailili, R.; Ji, H. W.; Wang, K. W.; Dong, X. A.; Chen, C. C.; Sheng, H.; Bahnemann, D. W.; Zhao, J. C. ZnO with Controllable Oxygen Vacancies for Photocatalytic Nitrogen Oxide Removal. *ACS Catal.* **2022**, *12*, 10004−10017.
(25) Wan, Y. S.; Li, J. B.; Ni, J. P.; Wang, C.; Ni, C. S.; Chen, H. Crystal-Facet and Microstructure Engineering in ZnO for Photocatalytic NO Oxidation. *J. Hazard. Mater.* **2022**, *435*, No. 129073.
(26) Zhou, X.; Xie, Z.-X.; Jiang, Z.-Y.; Kuang, Q.; Zhang, S.-H.; Xu, T.; Huang, R.-B.; Zheng, L.-S. Formation of ZnO Hexagonal Micro-pyramids: A Successful Control of the Exposed Polar Surfaces with the Assistance of An Ionic Liquid. *Chem. Commun.* **2005**, 5572−5574.
(27) Jiang, Z.-Y.; Xu, T.; Xie, Z.-X.; Lin, Z.-W.; Zhou, X.; Xu, X.; Huang, R.-B.; Zheng, L.-S. Molten Salt Route toward the Growth of ZnO Nanowires in Unusual Growth Directions. *J. Phys. Chem. B* **2005**, *109*, 23269−23273.
(28) Welton, T. Room-temperature Ionic Liquids: Solvents for Synthesis and Catalysis. *Chem. Rev.* **1999**, *99*, 2071−2084.
(29) Hailili, R.; Bahnemann, D. W.; Schneider, J. Ionic liquid-mediated Microstructure Regulations of Layered Perovskite for Enhanced Visible Light Photocatalytic Activity. *Front. Catal.* **2022**, *2*, No. 890842.
(30) Pei, Y. C.; Zhang, Y. X.; Ma, J.; Fan, M. H.; Zhang, S. J.; Wang, J. J. Ionic Liquids for Advanced Materials. *Mater. Today Nano* **2022**, *17*, No. 100159.
(31) Ren, F.; Wang, J. W.; Xie, F. W.; Zan, K.; Wang, S.; Wang, S. J. Applications of Ionic Liquids in Starch Chemistry: A Review. *Green Chem.* **2020**, *22*, 2162−2183.
(32) Yu, W. L.; Xu, D. F.; Peng, T. Y. Enhanced Photocatalytic Activity of g-$C_3N_4$ for Selective $CO_2$ Reduction to $CH_3OH$ via Facile Coupling of ZnO: A Direct Z-scheme Mechanism. *J. Mater. Chem. A* **2015**, *3*, 19936−19947.
(33) Zheng, Y. H.; Chen, C. Q.; Zhan, Y. Y.; Lin, X. Y.; Zheng, Q.; Wei, K. M.; Zhu, J. F.; Zhu, Y. J. Luminescence and Photocatalytic Activity of ZnO Nanocrystals: Correlation between Structure and Property. *Inorg. Chem.* **2007**, *46*, 6675−6682.
(34) Chen, D. M.; Wang, Z. H.; Ren, T. Z.; Ding, H.; Yao, W. Q.; Zong, R. L.; Zhu, Y. F. Influence of Defects on the Photocatalytic Activity of ZnO. *J. Phys. Chem. C* **2014**, *118*, 15300−15307.
(35) Tan, H. Q.; Zhao, Z.; Zhu, W.-B.; Coker, E. N.; Li, B. S.; Zheng, M.; Yu, W. X.; Fan, H. Y.; Sun, Z. C. Oxygen Vacancy Enhanced Photocatalytic Activity of Pervoskite $SrTiO_3$. *ACS Appl. Mater. Interfaces* **2014**, *6*, 19184−19190.
(36) Geng, Z. Q.; Kong, X. D.; Chen, W. W.; Su, H. Y.; Liu, Y.; Cai, F.; Wang, G. X.; Zeng, J. Oxygen Vacancies in ZnO Nanosheets Enhance $CO_2$ Electrochemical Reduction to CO. *Angew. Chem., Int. Ed.* **2018**, *57*, 6054−6059.
(37) Peng, S. Q.; Gan, C.; Yang, Y.; Ji, S. F.; Li, Y. X. Low Temperature and Controllable Formation of Oxygen Vacancy $SrTiO_{3-x}$ by Loading Pt for Enhanced Photocatalytic Hydrogen Evolution. *Energy Technol.* **2018**, *6*, 2166−2171.
(38) Wang, J. P.; Wang, Z. Y.; Huang, B. B.; Ma, Y. D.; Liu, Y. Y.; Qin, X. Y.; Zhang, X. Y.; Dai, Y. Oxygen Vacancy Induced Band-Gap Narrowing and Enhanced Visible Light Photocatalytic Activity of ZnO. *ACS Appl. Mater. Interfaces* **2012**, *4*, 4024−4030.
(39) Guo, H.-L.; Zhu, Q.; Wu, X.-L.; Jiang, Y.-F.; Xie, X.; Xu, A.-W. Oxygen Deficient $ZnO_{1-x}$ Nanosheets with High Visible Light Photocatalytic Activity. *Nanoscale* **2015**, *7*, 7216−7223.
(40) Kubelka, P.; Munk, F. An Article on Optics of Paint Layers. *Z. Technol. Phys.* **1930**, *12*, 593−601.
(41) Xu, Y.; Schoonen, M. A. A. The Absolute Energy Positions of Conduction and Valence Bands of Selected Semiconducting Minerals. *Am. Miner.* **2000**, *85*, 543−556.
(42) Zhang, Y. C.; Du, Z. N.; Li, W. K.; Zhang, M.; Dionysiou, D. D. High-Performance Visible-Light-Driven $SnS_2/SnO_2$ Nanocomposite Photocatalyst Prepared via In situ Hydrothermal Oxidation of $SnS_2$ Nanoparticles. *ACS Appl. Mater. Interfaces* **2011**, *3*, 1528−1537.
(43) Hailili, R.; Wang, Z. Q.; Xu, M. Y.; Wang, Y. H.; Gong, X. Q.; Xu, T.; Wang, C. Y. Layered Nanostructured Ferroelectric Perovskite $Bi_5FeTi_3O_{15}$ for Visible-light Photodegradation of Antibiotics. *J. Mater. Chem. A* **2017**, *5*, 21275−21290.


https://doi.org/10.1021/acsami.3c02286
*ACS Appl. Mater. Interfaces* 2023, 15, 23185−23198

(44) Hailili, R.; Wang, C. Y.; Lichtfouse, E. Perovskite Nanostructures Assembled in Molten Salt Based on Halogen Anions KX (X = F, Cl and Br): Regulated Morphology and Defect-Mediated Photocatalytic Activity. *Appl. Catal., B* **2018**, *232*, 531−543.
(45) He, W. W.; Kim, H.-K.; Wamer, W. G.; Melka, D.; Callahan, J. H.; Yin, J.-J. Photogenerated Charge Carriers and Reactive Oxygen Species in ZnO/Au Hybrid Nanostructures with Enhanced Photocatalytic and Antibacterial Activity. *J. Am. Chem. Soc.* **2014**, *136*, 750−757.
(46) Shang, H.; Li, M. Q.; Li, H.; Huang, S.; Mao, C. L.; Ai, Z. H.; Zhang, L. Z. Oxygen Vacancies Promoted the Selective Photocatalytic Removal of NO with Blue $TiO_2$ via Simultaneous Molecular Oxygen Activation and Photogenerated Hole Annihilation. *Environ. Sci. Technol.* **2019**, *53*, 6444−6453.
(47) Zhang, M.; Averseng, F.; Krafft, J.-M.; Borghetti, P.; Costentin, G.; Stankic, S. Controlled Formation of Native Defects in Ultrapure ZnO for the Assignment of Green Emissions to Oxygen Vacancies. *J. Phys. Chem. C* **2020**, *124*, 12696−12704.
(48) Panigrahy, B.; Aslam, M.; Misra, S. D.; Ghosh, M.; Bahadur, D. Defect-Related Emissions and Magnetization Properties of ZnO Nanorods. *Adv. Funct. Mater.* **2010**, *20*, 1161−1165.
(49) Motaung, D. E.; Mhlongo, G. H.; Nkosi, S. S.; Malgas, G. F.; Mwakikunga, B. W.; Coetsee, E.; Swart, H. C.; Abdallah, H. M. I.; Moyo, T.; Ray, S. S. Shape-Selective Dependence of Room Temperature Ferromagnetism Induced by Hierarchical ZnO Nanostructures. *ACS Appl. Mater. Interfaces* **2014**, *6*, 8981−8995.
(50) Vitiello, G.; Iervolino, G.; Imparato, C.; Rea, I.; Borbone, F.; Stefano, L. D.; Aronne, A.; Vaiano, V. F-doped ZnO Nano- and Meso-crystals with Enhanced Photocatalytic Activity in Diclofenac Degradation. *Sci. Total Environ.* **2021**, *762*, No. 143066.
(51) Li, H.; Shang, H.; Li, Y. H.; Cao, X. M.; Yang, Z. P.; Ai, Z. H.; Zhang, L. Z. Interfacial Charging−Decharging Strategy for Efficient and Selective Aerobic NO Oxidation on Oxygen Vacancy. *Environ. Sci. Technol.* **2019**, *53*, 6964−6971.
(52) Huang, H. W.; Zhou, C.; Jiao, X. C.; Yuan, H. F.; Zhao, J. W.; He, C. Q.; Hofkens, J.; Roeffaers, M. B. J.; Long, J. L.; Steele, J. A. Subsurface Defect Engineering in Single-Unit-Cell $Bi_2WO_6$ Monolayers Boosts Solar-Driven Photocatalytic Performance. *ACS Catal.* **2020**, *10*, 1439−1443.
(53) Zhang, Q.; Huang, Y.; Peng, S. Q.; Zhang, Y. F.; Shen, Z. X.; Cao, J.-J.; Ho, W. K.; Lee, S. C.; Pui, D. Y. H. Perovskite $LaFeO_3$-$SrTiO_3$ Composite for Synergistically Enhanced NO Removal under Visible Light Excitation. *Appl. Catal., B* **2017**, *204*, 346−357.





https://doi.org/10.1021/acsami.3c02286
*ACS Appl. Mater. Interfaces* 2023, 15, 23185−23198